Level-set segmentation of pulmonary nodules in radiographs using a CT prior

Jay S. Schildkraut[*a], Shoupu Chen[a], Michael Heath[a], Walter G. O'Dell[b], Paul Okunieff[b], M. C. Schell[b], and Narinder Paul[c]
[a]Carestream Health, Inc., 1049 Ridge Road West, Rochester, NY, USA 14615;
[b]Department of Radiation Oncology, University of Rochester Medical Center, 601 Elmwood Ave., Rochester, NY, USA 14642;
[c]Department of Radiology, Toronto General Hospital, 200 Elizabeth St., Toronto, Canada M5G 2C4

ABSTRACT

This research addresses the problem of determining the location of a pulmonary nodule in a radiograph with the aid of a pre-existing computed tomographic (CT) scan. The nodule is segmented in the radiograph using a level set segmentation method that incorporates characteristics of the nodule in a digitally reconstructed radiograph (DRR) that is calculated from the CT scan. The segmentation method includes two new level set energy terms. The contrast energy seeks to increase the contrast of the segmented region relative to its surroundings. The gradient direction convergence energy is minimized when the intensity gradient direction in the region converges to a point. The segmentation method was tested on 23 pulmonary nodules from 20 cases for which both a radiographic image and CT scan were collected. The mean nodule effective diameter is 22.5 mm. The smallest nodule has an effective diameter of 12.0 mm and the largest an effective diameter of 48.1 mm. Nodule position uncertainty was simulated by randomly offsetting the true nodule center from an aim point. The segmented region is initialized to a circle centered at the aim point with a radius that is equal to the effective radius of the nodule plus a 10.0 mm margin. When the segmented region that is produced by the proposed method is used to localize the nodule, the average reduction in nodule-position uncertainty is 46%. The relevance of this method to the detection of radiotherapy targets at the time of treatment is discussed.

Keywords: level-set segmentation, digital radiography, pulmonary nodule, computed tomography, radiation oncology, computer-aided detection, digitally reconstructed radiograph

1. INTRODUCTION

The automatic localization of an object in a radiograph is of practical importance because it can enable radiography to be used for near real-time object detection and localization during medical procedures, such as radiotherapy of pulmonary nodules. However, the segmentation of an object in a radiograph is generally very difficult to achieve because a radiographic image is a superposition of the radio densities of all material in the path of the X-ray beam. Structures that overlap and surround the object of interest often confound segmentation methods. However, when prior images of the object are available, such as a 3D medical image that contains the object, powerful segmentation methods can be used that incorporate the prior information.[1–4] The purpose of this paper is to describe a method that was developed for the segmentation of pulmonary nodules in radiographs using computed tomography (CT) scans as prior images.

In the segmentation method, the contour of the segmented region in a radiograph is represented by a level-set function (LSF).[5] An energy is defined that depends on the LSF and its derivatives, which is minimized when the contour of the segmented region matches the contour of the nodule. The calculus of variations is used to derive evolution equations that iteratively modify the LSF to reduce the energy. Included in the energy is a prior energy term that is minimized when the contour matches the contour of the nodule in a digitally reconstructed radiograph (DRR), which is calculated from a CT scan. In addition, the segmentation method includes two new level-set energy terms. The "contrast energy" seeks to increase the contrast of the segmented region relative to its surroundings. The "gradient direction convergence" (GDC) energy is minimized when the intensity gradient direction in the region converges to a point. The segmentation method was tested on 23 pulmonary nodules from 20 cancer cases for which both a radiographic image and CT scan were collected.

[*] jay.schildkraut@carestreamhealth.com; 585-627-8623; carestreamhealth.com

The method of nodule segmentation is outlined in Figure 1. The steps on the left side of the figure occur in a planning phase. In the first step in the planning phase a CT scan of the patient is acquired that includes the nodule. In the next step, the boundary of the nodule is delineated in each CT slice in which it appears. Next, a DRR is computed from the CT scan data using the location of a simulated source and detector that matches the geometry of the radiographic system that is used in the treatment phase. In the calculation of the DRR a record is maintained of the X-rays that pass through the nodule. This information is then used to produce a contour of the projection of the nodule in the DRR. In the last step in the planning phase a LSF is calculated for a region that corresponds to the nodule's projection in the DRR. This LSF is used as the prior LSF in the segmentation method.

The steps of the treatment phase are shown on the right side of Figure 1. In the first step a radiograph is captured of the region around the nodule. The radiograph is preprocessed in the next step in order to facilitate the nodule segmentation process. In the following step a LSF is initialized that corresponds to a circular region in the radiograph that is centered at a point that is the expected location of the nodule. The purpose of the next series of steps in the treatment phase is to evolve this LSF until it defines a contour that matches the actual contour of the nodule.

The evolution of the LSF for the radiograph is divided into coarse and fine steps. In the coarse step energy terms are minimized that are useful even when the current region contour is far from the contour of the nodule. A new energy term that is used in this step is the contrast energy, which is described below. The coarse segmentation step often results in more than one connected region. For this reason, it is followed by a step in which a single connected region that best matches the prior is selected, and the LSF is reinitialized for the contour of the selected region.

The purpose of the fine LSF evolution step is to provide an accurate contour for the nodule that precisely determines its position in the image. In this step energy terms are minimized that are of value when the current region contour is close to the actual contour of the nodule. An important energy term in this step is the GDC energy that is described below. The fine LSF evolution step results in a preliminary contour of the nodule region. This mask is processed further in a post-processing step in order to obtain the final region contour.

2. MATERIALS

2.1 CT scans

CT scans of pulmonary nodule cases were obtained from Toronto General Hospital. The images were captured with a GE Medical Systems LightSpeed QX/i scanner. The slice thickness is 5.0 mm, slice spacing 5.0 mm, in-slice pixel spacing 0.703 mm, and peak voltage 120 kV. Nodule contours were manually delineated using a drawing tool for each slice in which the nodule appears. The effective diameter of a nodule is estimated based on the nodule's volume in the CT scan using the equation,

$$d_e = 2\left(\frac{3V}{4\pi}\right)^{1/3}, \tag{1}$$

where V is the volume of the nodule in the CT scan. The effective diameter of the nodules is listed in the second column of Table 2.

2.2 Radiography

Posterior-anterior (PA) chest radiographs of the pulmonary nodule cases were obtained from Toronto General Hospital. Radiographs were captured with a Kodak DirectView CR system. The digitized radiographs have an inter-pixel spacing of 0.168 mm. The location of nodules in the radiographs (radiograph nodule truth) was manually delineated using a drawing tool with the guidance of a board-certified radiologist. All processing was preformed on an 80.0 × 80.0 mm region of interest (ROI) in the radiograph. The ROIs are selected based on the location of a nodule in the radiograph as described below.

3. METHODS

3.1 DRR calculation

The method that is used to calculate DRRs is as described by Sherouse.[6] X-rays are traced from a simulated source point to each pixel in a simulated detector through the CT data. The CT value at an X-ray point is obtained by trilinear interpolation of the CT values at the eight corner points of the voxel that contains the point. In the DRR generation process, a record is made of X-rays that pass through the nodule and the amount of density the nodule contributes to the integral density along each X-ray. The pixels in the DRR that are associated with X-rays that pass through the nodule define the region of the nodule's projection in the DRR.

3.2 Preprocessing the radiograph

The radiograph is preprocessed in order to remove low-frequency intensity gradients and achieve a standard intensity mean and standard deviation. The removal of low-frequency intensity gradients increases the robustness of downstream processing. Low-frequency intensity gradients are removed by fitting the image intensities to a third-order bivariate polynomial. This polynomial is then subtracted from the image. Next, a linear transformation is applied to the intensities of the difference image that results in an image with a mean intensity of 2000 and intensity standard deviation of 600. The nodules are then enhanced relative to normal anatomy by the application of gray-scale morphological operations using Gaussian and bone-like templates .[28]

3.3 Level-set segmentation theory

3.3.1 Minimization of energy integral with levels sets

In the image domain Ω, the segmented region R is represented by a LSF $\phi(x, y)$ using the convention that $\phi(x, y) > 0$ inside the region. Two methods are commonly used to evolve the LSF from its initial state to a function with zero level set $\phi(x, y) = 0$ at the desired region contour. Sethian uses an equation of motion that drives movement of the contour at a velocity that approaches zero as the desired contour is reached.[7] Alternatively, Chan and Vese define an energy in terms of the level-set function that is minimized when the zero level set is at the desired contour.[8] In this work the energy minimization approach to level-set segmentation is used.

An energy is defined that is dependent on the segmented region R, the radiographic image data $I(x, y)$, and the characteristics of the prior, which in this case, is the nodule in a DRR that is calculated from the CT scan. The segmentation process requires finding the LSF that minimizes this energy. With the exception of energy terms that depend on the prior, the energy terms are of the form,

$$E = \iint_{\Omega} f(\phi, \phi_x, \phi_y, x, y)\,dxdy \quad . \tag{2}$$

This integral is minimized with respect to $\phi(x, y)$ using the calculus of variations for the case of several independent variables.[9] Application of the calculus of variations to Eq. (2) leads to the partial differential equation (PDE) for the evolution of the LSF,

$$\frac{\partial \phi(x, y)}{\partial t} = -\left(\frac{\partial f}{\partial \phi} - \frac{\partial}{\partial x}\frac{\partial f}{\partial \phi_x} - \frac{\partial}{\partial y}\frac{\partial f}{\partial \phi_y} \right) \quad . \tag{3}$$

3.3.2 Contrast energy

Segmentation methods that involve energy minimization often use the Mumford-Shah energy, which is minimized when the image inside and outside a region R are homogeneous.[10,11] The integrand for this energy is,

$$f(x,y) = \left|I(x,y) - I_{in}^{\text{avg}}\right|^2 H(\phi(x,y)) + \left|I(x,y) - I_{out}^{\text{avg}}\right|^2 \left(1 - H(\phi(x,y))\right), \tag{4}$$

where I_{in}^{avg} is the average image intensity within R, I_{out}^{avg} is the average intensity outside R, and $H(z)$ is the Heaviside function. Inserting Eq. (4) into Eq. (3) results in the evolution equation for the Mumford-Shah energy,

$$\frac{\partial \phi(x,y)}{\partial t} = -\left|I(x,y) - I_{in}^{\text{avg}}\right|^2 \delta(\phi(x,y)) + \left|I(x,y) - I_{out}^{\text{avg}}\right|^2 \delta(\phi(x,y)), \tag{5}$$

where $\delta(z)$ is the delta function.

The Mumford-Shah energy is not suitable for the segmentation of a nodule in a radiograph because the image intensity in the nodule region is usually not homogenous because of overlapping tissue. In addition, a region-based energy should take into account that nodules have positive contrast relative to their surroundings. In place of the Mumford-Shah energy, the region-based contrast energy is introduced, which is minimized when the segmented region has a positive contrast relative to its surroundings. The contrast energy has the integrand,

$$f(x,y) = \left|I(x,y) - I_{in}^{\text{high}}\right|^2 H(\phi(x,y)) + \left|I(x,y) - I_{out}^{low}\right|^2 \left(1 - H(\phi(x,y))\right), \tag{6}$$

where I_{in}^{high} is the intensity at 2.0% penetration at the top of the histogram of intensities inside the region, and I_{out}^{low} is the intensity at 2.0% penetration at the bottom of the histogram of intensities outside the region. Using histograms to determine extreme intensity values, rather than using minimum and maximum values, makes the contrast energy less susceptible to image noise. Inserting Eq. (6) into Eq. (3) results in the evolution equation for the contrast energy,

$$\frac{\partial \phi(x,y)}{\partial t} = -\left|I(x,y) - I_{in}^{\text{high}}\right|^2 \delta(\phi(x,y)) + \left|I(x,y) - I_{out}^{low}\right|^2 \delta(\phi(x,y)). \tag{7}$$

3.3.3 Gradient direction convergence energy

As discussed above, a nodule in a radiograph is often obscured by overlapping tissue, which results in a large variation of intensity in the nodule region. For example, if a rib partially overlaps with the nodule, the intensity will be much greater inside the overlapped region than outside the overlapped region. Researchers in the field of computer-aided detection of pulmonary nodules have developed features for nodule detection that minimize the effect of overlapping tissue. One of the most robust features for nodule detection is the convergence of the image's intensity gradient direction to a central region.[12] The gradient within an approximately spherical nodule points to the nodule's center, even when a portion of the nodule overlaps with a structure that has approximately uniform density, such as a rib. This feature is added to the segmentation method in the form of an energy term that decreases when the gradient at locations inside R are directed towards a point. The energy integrand for this GDC energy is,

$$f(x,y) = -\cos\left[\theta_{gr}(x,y) - \theta_o(x,y)\right] H(\phi(x,y)), \tag{8}$$

where $\theta_{gr}(x, y)$ is the direction of the image intensity gradient at location (x, y) and $\theta_o(x, y)$ is the direction from the point (x, y) to (x_o, y_o). The point (x_o, y_o) is set at the center of the segmented region and is updated as the region evolves. Inserting Eq. (8) into Eq. (3) results in the evolution equation for the GDC energy,

$$\frac{\partial \phi(x,y)}{\partial t} = \cos\left[\theta_{gr}(x,y) - \theta_o(x,y)\right] \delta(\phi(x,y)) \quad . \tag{9}$$

3.3.4 Curvature energy

The purpose of the curvature energy is to penalize regions with a complicated contour. The energy integrand for the curvature energy is,

$$f(x, y) = \left|\nabla H(\phi(x, y))\right| . \tag{10}$$

Inserting Eq. (10) into Eq. (3) results in the evolution equation,

$$\frac{\partial \phi(x,y)}{\partial t} = \delta(\phi(x,y))\, div\left(\frac{\nabla \phi(x,y)}{\left|\nabla \phi(x,y)\right|}\right) . \tag{11}$$

3.3.5 Prior energy

The prior energy term is minimized when the LSF for the segmented region in the radiograph matches the registered LSF for the nodule in the DRR. The symmetric prior energy of Cremers and Soatto is used, which has the integrand,[1]

$$f(x,y) = \{\phi(x,y) - \phi_p(x_p, y_p)\}^2 \frac{h(\phi(x,y)) + h(\phi_p(x_p, y_p))}{2} , \tag{12}$$

where ϕ_p is the LSF of the prior, and $h(\phi)$ is a the normalized Heaviside function,

$$h(\phi) = \frac{H(\phi)}{\iint_{\Omega} H(\phi)\,dxdy} . \tag{13}$$

The segmentation of a nodule in the radiograph using this prior energy term is a joint segmentation-registration process. This is seen in Eq. (12), where the LSF of the prior depends on coordinates $x_p(x, y)$ and $y_p(x, y)$ in the domain Ω_p of the prior DRR image, which are related to coordinates (x, y) in the radiograph by a rotation and translation, which has the general form,

$$\begin{bmatrix} x_p \\ y_p \end{bmatrix} = \vec{g}(x, y, \theta, t_x, t_y) , \tag{14}$$

where θ is the angle of rotation, and t_x and t_y are the components of the translation vector.

The evolution equation for the LSF for the energy integrand in Eq. (12) is,

$$\frac{\partial \phi(x,y)}{\partial t} = -(\phi - \phi_p)\{h(\phi) + h(\phi_p)\}$$
$$-\frac{\delta(\phi)}{2\iint_\Omega H(\phi)dxdy}\left[(\phi-\phi_p)^2 - \iint_\Omega (\phi-\phi_p)^2 h(\phi)dxdy\right]. \tag{15}$$

The parameters θ, t_x, and t_y in the registration transform in Eq. (14) also have associated evolution equations that are obtained by taking the derivative of the prior energy with respect to each parameter and using the gradient decent method to minimize the energy. The evolution equation for θ is,

$$\frac{\partial \theta}{\partial t} = \iint_\Omega (\phi-\phi_p)\{h(\phi)+h(\phi_p)\}\mathrm{K}_\theta dxdy$$
$$-\frac{1}{2\iint_\Omega H(\phi_p)dxdy}\iint_\Omega \{(\phi-\phi_p)^2 - \overline{(\phi-\phi_p)}^2\}\delta(\phi_p)\mathrm{K}_\theta dxdy, \tag{16}$$

where

$$\overline{(\phi-\phi_p)}^2 = \iint_\Omega (\phi-\phi_p)^2 h(\phi_p)dxdy, \tag{17}$$

and

$$\mathrm{K}_\theta = \frac{\partial \phi_p}{\partial x}\frac{\partial g_x}{\partial \theta} + \frac{\partial \phi_p}{\partial y}\frac{\partial g_y}{\partial \theta}, \tag{18}$$

where g_x and g_y are the x- and y-component of the vector **g**, respectively. The evolution equation for t_x, and t_y are identical to Eqs. (16)–(18) with t_x and t_y substituted for θ.

3.3.6 Contraction energy

A contraction energy is added so that the initial contour has a tendency to decrease in area. The integrand for the contraction energy is,

$$f(x,y) = H(\phi(x,y)). \tag{19}$$

Inserting Eq. (18) into Eq. (3) results in the evolution equation,

$$\frac{\partial \phi(x,y)}{\partial t} = -\delta(\phi(x,y)). \tag{20}$$

3.4 Level-set segmentation implementation

3.4.1 Image preparation

In order to reduce image noise, the full-resolution image is blurred with a Gaussian filter before segmentation. The filter size is 9 × 9 pixels, and the Gaussian distribution has a standard deviation of 7.0 pixels.

3.4.2 Heaviside and delta functions

In level-set implementations, a regularized Heaviside function is used that has a finite transition between zero and one. In our implementation the function used is,

$$H(z) = \frac{1}{2}\left[1 + \frac{2}{\pi}\tan^{-1}\left(\frac{z}{\varepsilon}\right)\right], \tag{21}$$

where ε is a constant that determines the width of the transition region. The delta function that is consistent with Eq. (21),

$$\delta(z) = \frac{\varepsilon}{\pi}\frac{1}{\varepsilon^2 + z^2}, \tag{22}$$

is obtained by taking the derivative with respect to z.

In the formulation of energy terms, the factor $\left(1 - H(\phi)\right)$ is used to define points that are outside the segmented region. In practice, it is necessary to further limit this outside region to points that immediately surround the segmented region; otherwise, statistical quantities, such as the low intensity outside the region in Eqs. (6) and (7), will depend on all image points regardless of the distance from the segmented region. Consequently, segmentation results will depend on the field of view of the processed radiograph. For this reason, the outside region is limited to points for which

$$\beta \le \phi(x, y) < 0, \tag{23}$$

where β is a negative constant.

3.4.3 Level-set function initialization

The initial segmented region in the radiograph is always initialized to a circle that is centered at the middle of the ROI image. In this case, the LSF is initialized to a signed distance function using the equation,

$$\phi(x, y) = r^2 - \sqrt{(x - x^c)^2 + (y - y^c)^2}, \tag{24}$$

where r is the radius of the initial region and (x^c, y^c) is the center of the region.

The LSF for the nodule region in the DRR image is initialized to a signed distance function by solving the differential equation,

$$\frac{\partial\phi(x, y, t)}{\partial t} = S\left(I_{mask}(x, y)\right)\left[1 - \left|\nabla\phi(x, y, t)\right|\right], \tag{25}$$

where I_{mask} is the mask of the nodule region in the DRR, and

$$S = \begin{Bmatrix} -1 & Outside\,Mask \\ 0 & Mask\,Boundary \\ +1 & Inside\,Mask \end{Bmatrix}. \tag{26}$$

The method of solving the differential Eq. (25) is described by Sussman et al.[13]

3.4.4 Transform between radiograph and DRR

The transform in Eq. (14) from the image domain of the radiograph Ω to the image domain of the DRR Ω_p is chosen to uncouple the evolution equations for θ, t_x, and t_y. The transformation used is:

$$\begin{bmatrix} x_p \\ y_p \end{bmatrix} = \begin{bmatrix} x_p^c + (x - x_p^c - t_x)\cos\theta + (y - y_p^c - t_y)\sin\theta \\ y_p^c - (x - x_p^c - t_x)\sin\theta + (y - y_p^c - t_y)\cos\theta \end{bmatrix}, \tag{27}$$

where (x_p^c, y_p^c) is the center of the prior shape. The inverse transformation of Eq. (27), which maps a point in the DRR to the radiograph, is a rotation around the center of the nodule in the DRR plus a translation.

3.4.5 Evolution of level-set function

In each time increment in the coarse and fine evolution steps of the LSF, the change in the function is a weighted sum of the time derivatives of $\phi\,(x, y)$ for each of the energies,

$$\frac{\partial \phi}{\partial t} = \begin{bmatrix} \lambda_{contrast}\left(\frac{\partial \phi}{\partial t}\right)_{contrast} + \lambda_{curvature}\left(\frac{\partial \phi}{\partial t}\right)_{curvature} + \lambda_{GDC}\left(\frac{\partial \phi}{\partial t}\right)_{GDC} \\ + \lambda_{prior}\left(\frac{\partial \phi}{\partial t}\right)_{prior} + \lambda_{contraction}\left(\frac{\partial \phi}{\partial t}\right)_{contraction} \end{bmatrix}, \tag{28}$$

where $\lambda_{contrast}$ is the weight for the contrast energy, $\lambda_{curvature}$ is the weight for the curvature energy, λ_{GDC} is the weight for the gradient direction convergence energy, λ_{prior} is the weight for the prior energy, and $\lambda_{contraction}$ is the weight for the contraction energy. The parameter values that are used in both steps are summarized in Table 1. The transform parameters θ, t_x, and t_y. in Eq. (27) are initialized to zero and updated in each time increment according to Eqs. (16)–(18) for θ and analogous equations for t_x and t_y.

LSF evolution ends when a time increment fails to change a specified energy. In the coarse LSF evolution step, a minimum of 50 and a maximum of 150 time increments are performed. After the minimum number of increments, if the contrast energy changes by less than 0.20% in a time increment, LSF evolution is stopped. In the fine LSF evolution step, a minimum of 5 and a maximum of 10 time increments are performed. After the minimum number of increments, if the GDC energy changes by less that 1.00% in a time increment, LSF evolution is stopped.

3.5 Region selection and level-set function reinitialization

The segmented region from the coarse LSF evolution step often consists of two or more disconnected regions. Furthermore, a single connected region may consist of several distinct regions that are connected by only a few bridge pixels. For this reason, before region selection, the segmented region mask is eroded by a binary morphological filter in order to break up slightly connected regions. The size of the morphological filter is set to 15% of the equivalent diameter (see Eq. (1)) of the prior in order to prevent the mask of a small nodule from being erased in the erosion process. Next, the connected region mask that has the highest normalized cross-correlation with the mask of the registered prior is selected, and all other regions are removed. The selected region is dilated by a binary morphological filter, which is the same size as the erosion filter, to undo the effect of the erosion on the selected region. Finally, the LSF is reinitialized to a signed distance function for the selected region using Eqs. (24) to (26).

3.6 Post-processing of the region mask

Post-processing occurs after the fine LSF evolution step. Because the input to this step is a connected region, and it only refines the region's contour, the output of this step is usually a single connected region. When this is not the case, region selection is again applied in this step. The step ends with a flood-fill operation in order to remove small holes in the region.

4. RESULTS

The method of level-set segmentation with a CT prior was tested on 23 nodules from 20 cancer cases for which both a CT scan and radiograph were collected. Figure 2 illustrates the steps in the method for nodules 9, 19, and 23 in the first, second, and third row, respectively. Column (a) shows a CT slice in which the nodule is visible with a green contour around the nodule. Column (b) shows the DRR with a blue contour outlining the projection of the nodule. Column (c) shows a ROI in the radiograph with a green contour around the true location of the nodule. In all cases, the true nodule center is horizontally and vertically displaced by 10 mm from the ROI center which is marked by a yellow dot. Column (d) shows the preprocessed ROI, with green truth contour. The initial segmented region contour is in red, and the initial prior contour is in blue. Column (e) shows the green truth contour, the final segmented region contour in red, and registered prior contour in blue.

The effectiveness of the proposed method for the reduction in the uncertainty of the location of a nodule in a radiograph was tested by running the segmentation method 100 times. For 9 of the runs, the aim point is on a 3 × 3 10 mm grid with the true nodule location at the grid's center. The other 81 times, the aim point is located at a random horizontal and

vertical displacement of between 0.0 and 10.0 mm from the nodule's center. The segmented region is initialized to a circle that is centered at the aim point with a radius equal to the effective radius of the nodule plus a 10.0 mm margin. The ROI is an 80 × 80 mm region of the radiograph with the aim point at its center. Figure 3 shows the segmentation results for nodule 4 for the 9 aim points on the 3 × 3 10 mm grid. The aim point at the center of the ROI is indicated by the yellow dot. The contours are as displayed in column (e) in Fig. 2.

The results of this experiment are shown in Table 2. The third column in Table 2, Seg. Region Overlap With True Nodule Region, is given by,

$$A_{overlap} \equiv \frac{2(A_{seg} \cup A_{truth})}{A_{seg} + A_{truth}}, \tag{29}$$

where A_{seg} is the area of the segmented region, and A_{truth} is the true nodule area.[14] The results are presented in the form of average ± standard deviation (minimum, maximum) values. Column 4, Nodule Position Offset (mm), is the distance between the true nodule center and the aim point. In all cases, the minimum distance is 0.0 mm and the maximum distance is 14.14 mm. Column 5, Seg. Region to Nodule Position Error (mm), is the distance between the center of the segmented region and the true nodule center. A measure of the effectiveness of the method is the average percent error reduction when the center of the segmented region is used as the nodule center instead of the aim point. This quantity is expressed as,

$$\mathrm{P}_{error\ reduction} \equiv 100 \frac{D^{avg}_{nodule-aim} - D^{avg}_{nodule-seg}}{D^{avg}_{nodule-aim}}, \tag{30}$$

where $D^{avg}_{nodule-aim}$ is the average distance between the true nodule center and aim point, and $D^{avg}_{nodule-seg}$ is the average distance between the true nodule center and center of the segmented region. The average percent error reduction is in column 6 of Table 2.

The treatment phase of the algorithm has a runtime of 12.74±3.25(7.00,22.00) seconds on a 2.33 GHz Intel® Core™2 Duo Desktop Processor E6550 with 3.48 GB of RAM for the set of 23 nodules.

5. DISCUSSION

Computer detection of pulmonary nodules in chest radiographs has been studied extensively.[15–17] Although, powerful image processing technology has been developed, the detection of nodules in radiographs is hampered by the superimposition of normal anatomy on the nodule and other tissue that can be mistaken for a nodule. For this reason, emphasis has shifted to computer detection of nodules in 3D medical images, such as CT scans, for which image reconstruction eliminates the superposition problem.[18,19] However, projection radiography still has advantages relative to CT, including lower radiation dose, faster image captures times, and simpler hardware. This research is motivated by the idea that, as 3D medical images become increasingly more available, the 3D images can serve to extend the applications of projection radiography. The information on an object of interest that is contained in a 3D image can be used to substantially overcome the superposition problem that is inherent in a projection radiograph. An example application is the use of a CT radiotherapy planning image to aid in the computer detection of the radiotherapy target in radiographs, which are captured during treatment.

The localization of pulmonary nodules during radiotherapy is of considerable interest because nodule motion caused by respiration results in an uncertainty of a nodule's location during treatment.[20] Nodule location uncertainty can be reduced by capturing the planning image and treating the tumor, all while the patient is in the same respiratory state. However, considerable margins are still required. For example, at the University of Rochester Medical Center, stereotactic radiation treatment of pulmonary nodules is performed using end-expiration breath holding with treatment margins of 7 × 7 × 10 mm. Using a variety of respiratory gating methods, many other treatment centers performing pulmonary SRT employ similar margins, typically 10 mm, to account for setup and positioning errors.[21]

Researchers have developed methods to decrease the uncertainty of pulmonary nodule location during treatment by radiographic imaging of the region of the target nodule.[22,23] One means of overcoming the difficulty of directly detecting

the location of the nodule is to implant metal markers nearby. The markers can then be tracked in real-time using a fluoroscope.[24] Recent work has focused on eliminating the need for implanted markers because of the evasiveness of the implantation procedure, and the motion of the markers may not be perfectly correlated with the motion of the nodule. Schweikard, Shiomi, and Adler captured a planning-phase CT image at inhalation and exhalation.[25] CT scans for intermediate respiratory states are obtained by interpolation. Pretreatment DRRs are calculated from the CT data sets. In the treatment phase, the DRRs are matched with radiographs that are captured periodically. The CT data set that was used to generate the best-matching DRR provides the location of the target.

The segmentation method that is described in this report can form the basis of another approach to nodule position detection. The CT scan provides information on the shape of the nodule, but nodule detection does not rely on a match between a DRR and a radiograph. A good match may not occur if the configuration of the patient differs in the planning and treatment phase. In addition, a method of target detection that uses segmentation, feature extraction, and classification, is inherently quicker and, therefore, better suited for near real-time applications than a method that relies on matching with a large number of reference images.

This segmentation method was tested on radiographs that were captured at normal incidence, because they were the only images available for this study. In a target-detection system for radiation therapy, the radiographs may be captured at oblique incidence. Radiographs that are captured at oblique angles have more problems with superposition of the anatomy on the nodule because of greater path length through the patient of the X-ray beam. However, this effect can be offset by optimizing the detectability of the nodule in the radiograph by configuring the radiographic system, based on an analysis of the CT scan, so that interference from superimposed tissue is minimized.[26,27]

6. CONCLUSION

A level-set segmentation method is described that successfully locates pulmonary nodules in a chest radiograph. In this method an energy term is used that compares the segmented region to the nodule in a DRR, which is calculated from an existing CT scan. Also, additional energy terms are introduced that depend on the contrast of the region and intensity-gradient direction convergence. The method was tested on 23 pulmonary nodules. An experiment was performed in which the region was initialized at points that were distributed about the true nodule center. The results of this experiment show that the segmentation method reduces uncertainty of nodule location by 46%.

REFERENCES

[1] D. Cremers and S. Soatto, "A Pseudo-distance for Shape Priors in Level Set Segmentation," 2nd IEEE Workshop on Variational, Geometric, and Level Set Methods in Computer Vision (2003).

[2] A. Yezzi, L. Zollei, and T. Kapur, "A variational framework for integrating segmentation and registration through active contours," Med. Image Anal. 7, 171-185 (2003).

[3] Y. Chen, W. Guo, F. Huang, D. Wilson, and E. A. Geiser, "Using prior shape and points in medical image segmentation," Lect. Notes Comput. Sc. 2683, 291-305 (2003).

[4] M. E. Leventon, O. Faugeras, W. E. L. Grimson, and W. M. Wells III, "Level set segmentation with intensity curvature priors," Proc. IEEE Workshop on Mathematical Methods in Biomedical Image Analysis, 4-11 (2000).

[5] [Geometric Level Set Methods], edited by S. Osher and N. Paragios, Springer Press, New York (2006).

[6] G. W. Sherouse, K. Novins, and E. L. Chaney, "Computation of digitally reconstructed radiographs for use in radiotherapy treatment design," J. Radiat. Oncol. Biol. Phys. 18, 651-658 (1990).

[7] J. A. Sethian, [Level Set Methods and Fast Marching Methods], 2nd ed., Cambridge University Press, Cambridge (1999).

[8] T. F. Chen and L. A. Vese, "Active contours without edges," IEEE T Image Proc. 10, 266-277 (2001).

[9] G. Arfken, [Mathematical Methods For Physicists], 3rd ed., Academic Press, Orlando, 942-943, (1985).

[10] D. Mumford and J. Shah, "Optimal approximation by piecewise smooth functions and associated variational problems," Commun. Pure Appl. Math. 42, 577-685 (1989).

[11] L. A. Vese and T. F. Chan, "A multiphase level set framework for image segmentation using the Mumford and Shah model," Int. J. Comput. Vision 50, 271-293 (2002).

[12] F. Mao, W. Qian, and L. P. Clarke, "Fractional dimension filtering for multiscale lung nodule detection," Proc. SPIE 3034, 449-456 (1997).

[13] M. Sussman, P. Smereka, and S. J. Osher, "A level set method for computing solutions to incompressible two-phase flow," J. Comput. Phys. 114, 146-159 (1994).
[14] F. Zhuge, G. D. Rubin, S. Sun, and S. Napel, "An Abdominal aortic aneurysm segmentation method: Level set with region and statistical information," Med. Phys. 33, 1440-1453 (2006).
[15] M. J. Carreira, D. Cabello, M. G. Penedo, and A. Mosquera, "Computer-aided diagnoses: Automatic detection of lung nodules," Med. Phys. 25, 1998-2006 (1998).
[16] B. Van Ginneken, B. M. Ter Haar Romeny, and M. A. Viergever, "Computer-aided diagnosis in chest radiography: A survey," IEEE T. Med. Imaging 20, 1228-1240 (2001)
[17] M. L. Giger, N. Ahn, K. Doi, H. MacMahon, and C. E. Metz, "Computerized detection of pulmonary nodules in digital chest images: Use of morphological filters in reducing false-positives," Med. Phys. 17, 861-865 (1990).
[18] Y. Lee, T. Hara, H. Fujita, S. Itoh, and T. Ishigaki, "Automated detection of pulmonary nodules in helical CT images based on an improved template-matching technique," IEEE T. Med. Imaging 20, 595-604 (2001).
[19] S. G. Armato III, M. L. Giger, and H. MacMahon, "Automated detection of lung nodules in CT scans: Preliminary results," Med. Phys. 28, 1552-1561 (2001).
[20] G. Hugo, C. Vargas, J. Liang, L. Kestin, J. W. Wong, and D. Yan, "Changes in the respiratory pattern during radiotherapy for cancer of the lung," Radiotherapy and Oncology 78, 326-331 (2006).
[21] W. G. O'Dell, M. C. Schell, D. Reynolds, P. Okunieff, "Dose broadening due to target position variability during fractionated breath-held radiation therapy," Med. Phys. 29, 1430-1437 (2002).
[22] R. I. Berbeco, S. B. Jiang, G. C. Sharp, G. T. Y. Chen, H. Mostafavi, and H. Shirato, "Integrated radiotherapy imaging system (IRIS): Design considerations of tumour tracking with linac gantry-mounted diagnostic x-ray systems with flat-panel detectors," Phys. Med. Biol. 49, 243-255 (2004).
[23] J. Chang, J. Sillanpaa, C. C. Ling, E. Seppi, E. Yorke, G. Mageras,and H. Arnois, "Integrated respiratory gating into a megavoltage cone-beam system," Med. Phys. 33, 2354-2361 (2006).
[24] T. Harada, H. Shirato, S. Ogura, S. Oizumi, K. Yamazaki, S. Shimizu, R. Onimaru, K. Miyasaka, M. Nishimura, and H. Dosaka-Akita, "Real-time tumor-tracking radiation therapy for lung carcinoma by the aid of insertion of a gold marker using bronchofiberscopy," Cancer 95, 1720-1727 (2002).
[25] A. Schweikard, H. Shiomi, and J. Adler, "Respiration tracking in radiosurgery without fiducials," Int. J. Med. Robot. Comp. 1, 19-27 (2005).
[26] J. S. Schildkraut, N. D. Cahill, S. Dhurjaty, and L. A. Ray, "Radiation therapy method with target detection," U.S. Patent No. 7453983, filed January 20, 2005.
[27] J. S. Schildkraut, M. D. Bedzyk, S. Chen, and T. J. Wojcik, "System for the real-time detection of targets for radiation therapy," U.S. Patent No. 7418079 filed May 23, 2006.
[28] J. S. Schildkraut, M. D. Heath, R. A. Senn, J. F. Revelli, Jr., and B. Luck, "Pulmonary nodule detection in a chest radiograph," U.S. Patent Publication 2007/0019852 filed July 22, 2005.

Table 1. Processing conditions and parameter values for coarse and fine steps of the level-set segmentation method.

Parameter	Coarse Steps	Fine Steps	Parameter	Coarse Steps	Fine Steps
ROI Size (mm)	80 × 80	80 × 80	$\lambda_{contaction}$	50	0
Pixel Spacing (mm)	0.336	0.168	λ_{GDC}	0	50
dt	1.0	1.0	$\lambda_{curvature}$	50	20
ε	3.00	3.00	λ_{prior}	1000	1000
β	-20.0	-20.0	Min/Max Time Increments	50/150	5/10
$\lambda_{contrast}$	2000	500	Stop Condition	<0.20% Energy Change	<1.0% Energy Change

Table 2. Nodule segmentation results for random nodule position offsets from an aim point.

Nodule	d_e (mm)	Seg. Region Overlap With True Nodule Region	Nodule Position Offset (mm)	Seg. Region to Nodule Position Error (mm)	% Nodule Position Error Reduction
1	20.75	79.51±1.65(73.74,81.83)	7.87±3.10	2.00±0.34(1.17, 2.85)	74.56
2	39.11	80.87±5.32(61.01,88.89)	7.67±3.14	4.65±1.79(0.98,10.78)	39.43
3	23.49	80.67±1.17(74.38,82.62)	8.16±2.99	2.24±0.06(1.99, 2.37)	72.52
4	21.96	80.00±1.33(78.04,86.18)	7.85±3.10	2.16±0.21(1.28, 2.62)	72.49
5	19.06	76.42±7.76(6.65,81.41)	8.00±3.01	1.27±1.14(0.40,12.08)	84.12
6	26.64	85.43±3.92(74.08,91.08)	8.40±2.85	2.33±1.01(0.27, 4.83)	72.21
7	13.88	69.48±15.41(0.00,79.46)	8.22±3.11	1.66±3.47(0.13,25.94)	79.81
8	26.42	76.05±11.35(22.83,87.77)	8.03±2.95	4.24±2.98(1.29,18.87)	47.15
9	21.03	61.47±3.95(41.66,68.36)	8.04±2.88	1.83±1.49(0.30, 8.85)	77.21
10	20.99	48.66±2.84(39.82,55.60)	7.53±3.10	4.62±1.51(0.56, 7.42)	38.65
11	29.23	75.02±7.20(17.38,82.71)	7.44±3.16	3.46±2.04(0.13,16.97)	53.57
12	19.11	40.25±34.95(0.00,87.15)	8.03±2.88	11.40±8.71(0.69,24.37)	-41.96
13	17.59	44.19±2.17(39.74,49.90)	7.71±3.08	3.69±0.24(3.06, 4.14)	52.17
14	31.13	56.66±7.08(44.81,76.03)	8.29±3.07	6.95±2.56(0.65,11.80)	16.18
15	12.07	42.34±34.13(0.00,91.40)	7.46±3.11	6.89±5.18(0.47,25.66)	7.68
16	48.19	66.49±4.56(51.75,73.50)	7.56±3.28	7.26±3.17(1.08,14.60)	3.93
17	28.95	69.27±10.36(40.68,82.99)	8.00±3.08	4.47±2.84(0.73,11.69)	44.08
18	14.54	46.98±6.04(29.93,61.53)	7.86±3.22	4.12±1.90(0.77, 9.31)	47.55
19	14.93	70.21±18.43(3.58,84.42)	8.31±3.04	3.42±2.79(1.49,14.36)	58.81
20	22.62	49.84±9.85(0.04,56.90)	7.54±3.27	7.55±2.63(4.77,22.16)	-0.10
21	15.27	78.11±2.15(72.44,83.03)	7.98±3.09	0.82±0.39(0.03, 1.63)	89.68
22	17.42	48.84±26.36(0.00,77.52)	8.03±3.32	7.93±8.84(1.71,26.53)	1.16
23	15.31	63.10±9.13(16.45,71.53)	7.85±3.20	2.52±2.60(0.03,14.64)	67.86
Avg	22.59	64.77	7.90	4.23	46.03

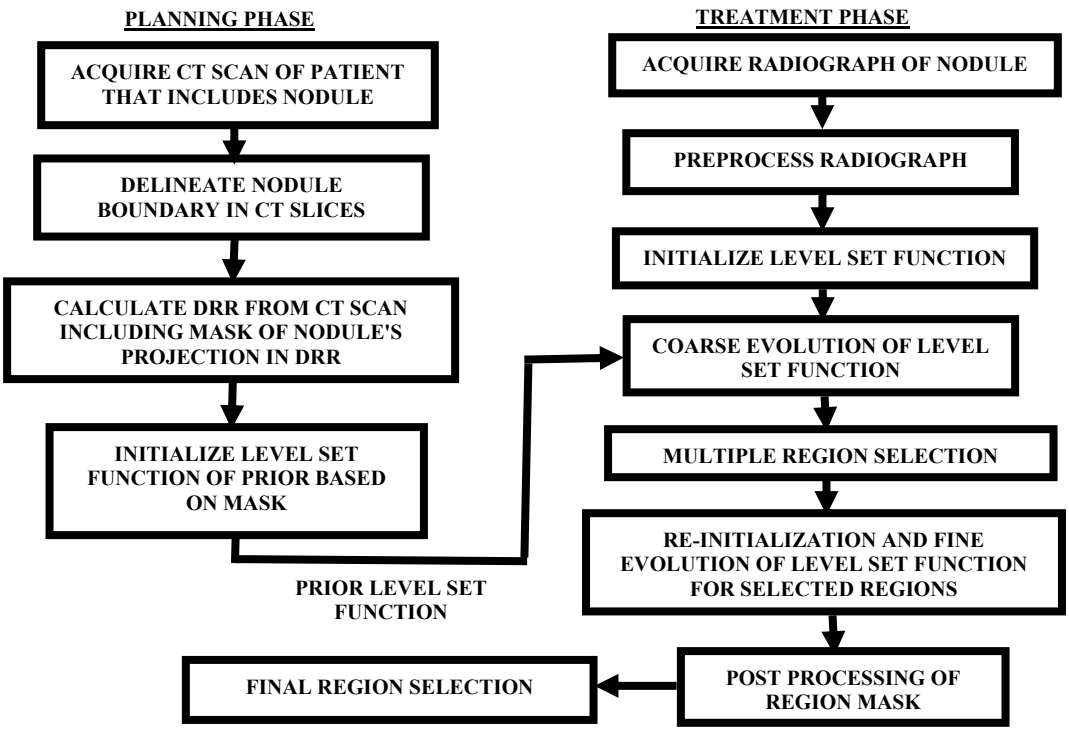

Fig. 1. Steps of the method for nodule detection in a radiograph using a CT prior.

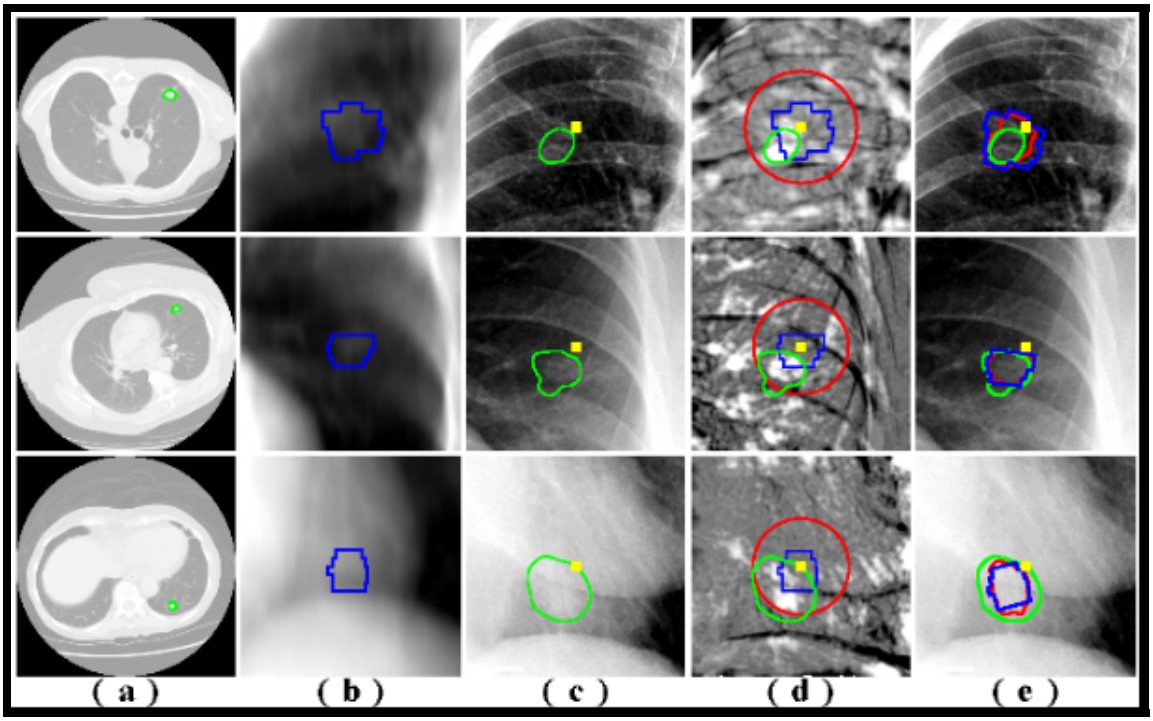

Fig. 2. Summary of processing steps for nodules 9, 19, and 23.

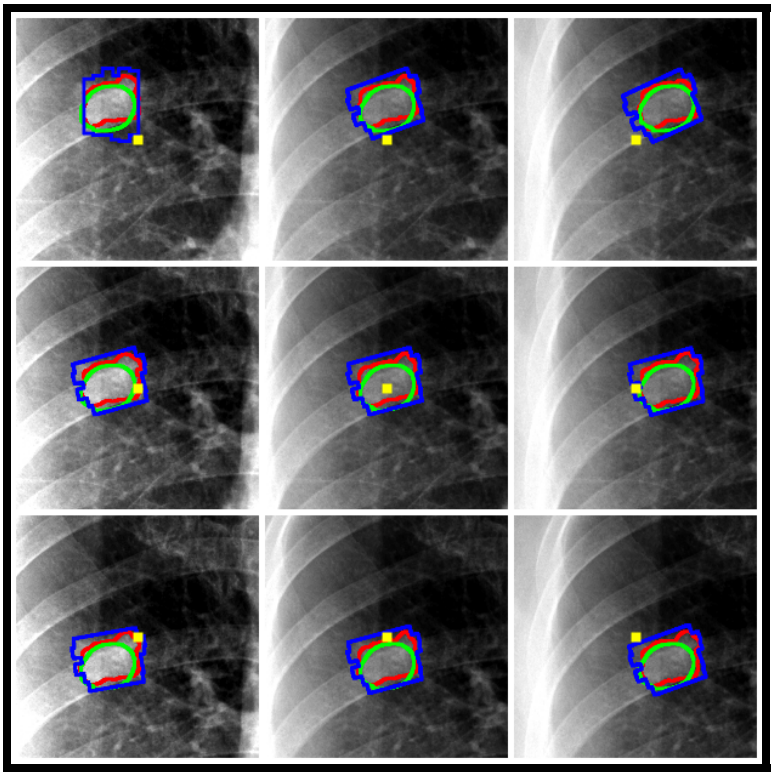

Fig. 3. Segmentation for 10 mm offsets from the aim point for nodule 4.